Journal of Superconductivity and Novel Magnetism ***22****, 797-804 (2009)*

Statistical Characterization and Process Control for Improved Growth of $La_{2-x}Sr_xCuO_4$ Films

J. A. Clayhold[1], O. Pelleg[2], A. T. Bollinger[2], G. Logvenov[2], B. M. Kerns[1], M. D. Schroer[1], D. W. Rench[1] and I. Bozovic[2]

[1]Department of Physics, Miami University, Oxford, Ohio 45056, USA
[2]Brookhaven National Laboratory, Upton, New York 11973-5000, USA

(Dated: May 21, 2009)

Abstract

We have used combinatorial molecular beam epitaxy (COMBE) technique to deposit thin cuprate films with continuous spread in chemical composition, as well as nominally uniform films. We have patterned them into linear pixel arrays and measured the transport properties of each pixel. We applied detailed statistical analysis to differentiate between various possible sources of random pixel-to-pixel variations, and utilized this knowledge to considerably tighten the process parameters and significantly reduce such variations. The density and quality of data points is high enough to allow detection of quantum phase transitions induced by tuning the chemical composition.

I. INTRODUCTION

The existence of quantum critical points in various condensed matter systems is an area of major interest to modern physics.[1-5] Just as in studies of classical critical phenomena, it is essential to have a high density of experimental points near the phase transition in order to properly characterize the critical exponents and the nature of the transition. In certain solid-solution materials including many complex oxides currently under intense study, quantum critical points are suspected to exist as a function of the chemical composition.[6-14] It thus becomes imperative to achieve high-resolution control of stoichiometry, but this is difficult if one sticks to traditional methods of synthesis of bulk materials, especially in single-crystal form.

We have embarked on a project to detect and characterize quantum phase transitions as a function of chemical composition in superconducting oxides.[10-14] Here, we focus on $La_{2-x}Sr_xCuO_4$ (LSCO), a high-temperature superconductor with the critical temperature reaching the maximum $T_c \approx 40$ K for $x \approx 0.15$. Our approach is to use the combinatorial molecular beam epitaxy (COMBE) with a continuous spread in chemical composition across the wafer. [15,16] We pattern such films into linear arrays of lithographically defined samples with minute pixel-to-pixel variations in composition. This is complemented by a high-throughput/high-precision characterization of such one-dimensional (1D) combinatorial sample libraries. [17] The technical goal is to increase the resolution of chemical composition (here, the Sr doping level) and the density of data points by a factor of hundred or more. The expectation is that this can reveal some discontinuities or kinks in one or more of the most relevant physical properties such as the

resistivity, the Hall coefficient, T_c, the superfluid density, etc., induced by tuning the chemical composition in a quasi-continuous manner.

We note that combinatorial synthesis techniques have been used extensively in search for new materials, both organic and inorganic [18,19]; in the complex oxide field, notable successes include discoveries of new phosphors [20,21], high-dielectric constant materials [22], ferroelectrics [23,24] and dilute magnetic semiconductors [25,26]. However, we are unaware of previous attempts to use this technique as a basic-research tool for studying quantum phase transitions.

In order to rule out experimental artifacts, one needs first to demonstrate the capability to reproducibly fabricate sample libraries uniform in chemical composition and without any jumps and kinks in the physical properties. Most of the present paper is focused on this first critical benchmark for our approach. Our goal is to control the absolute variation of chemical composition to within 0.1%; no previous reports of oxide film growth imposed so stringent requirements on spatial homogeneity. This is a big demand not just on the film synthesis but also on every step along the process chain, including cooling the sample down after growth, its subsequent annealing in ozone, various steps in the lithographic process, sample characterization by physical property measurements, as well as substrate and sample handling. A misstep anywhere in this chain can cause substantial, random, pixel-to-pixel variations of extrinsic origin, which make the sample unusable for the present purpose.

Our first test samples displayed lateral uniformity of the resistance and the Hall coefficient of better than 5%. In order to improve the sample growth and processing, it was necessary to look within that small 5% variation window for clues to improving the process. For this, we had to develop new measurement techniques and, just as important, new statistical measures of sample quality. These tools have made it possible to quantify and differentiate the deleterious effects of variations in (i) the pixel geometry, including the film thickness and lithographically defined dimensions, (ii) the sample stoichiometry including in particular the oxygen content, (iii) defects and impurity scattering, and (iv) the contact resistance. In this way, we were able, first, to resolve the physical origin of pixel-to-pixel variations in measured properties, and second, to tighten the process control and reduce such variations by over an order of magnitude. With this we have reached our first milestone on the path of COMBE search for quantum critical transitions in LSCO and other strongly-correlated electron materials of interest.

II. FILM GROWTH AND PROCESSING

For film synthesis we employed a unique atomic layer-by-layer molecular beam epitaxy (ALL-MBE) system equipped with advanced tools for in-situ surface analysis including reflection high energy electron diffraction and time-of-flight ion scattering spectroscopy. Although main aspects of our ALL-MBE deposition system have been described elsewhere [15], it is useful here to briefly recapitulate some of its basic features. The system has 16 elemental metal sources aimed at a shallow angle (20^0) with respect to the substrate. Since the deposition rate is higher on the substrate side nearer to the metal source, it is possible to deposit epitaxial thin oxide films with substantial continuous combinatorial spread in the chemical composition. [15, 16] On the other hand, by using two sources of the same element placed in opposition and with matched deposition rates, it is also possible to synthesize films which are remarkably uniform.

The actual deposition rate gradients can be measured in situ by a built-in scanning quartz crystal rate monitor (QCM). [15]

The system contains a second large vacuum chamber devoted to in-situ lithographic processing, including ion-beam etching and electron-beam deposition of metallic and insulating layers. This chamber is installed in a clean room; substrates can be prepared in a class 100 clean environment and loaded into the system without surface contamination. The growth chamber and the processing chambers are connected via a transfer chamber, and the samples can be shuttled from one to another without breaking vacuum. [15]

Using ALL-MBE we reproducibly fabricate single crystal films of cuprates and other complex oxides with atomically smooth surfaces and interfaces; the typical surface roughness estimated from atomic-force microscope images is 0.2-0.5 nm. [27-32] For this study we deposited a number of single-phase films with different Sr content. The films were grown on single crystal $LaSrAlO_4$ (LSAO) substrates polished with the surface perpendicular to the (001) crystallographic direction. The films were patterned using optical photoresist and ion milling or chemical etching as required. The pattern layout is shown in Fig. 1. The width of the central strip is 300 μm and the typical film thickness is 50 nm. The electrical current is applied along the central strip. The current and voltage contact pads form an 8 by 8 square array that allows for simultaneous measurements of resistance at 30 distinct locations and of the Hall effect at 31 distinct locations on the wafer, with 300 μm spacing between the pixels.

III. HIGH-DENSITY TRANSPORT MEASUREMENTS

We have constructed a specialized combinatorial transport measurement system capable of measuring both the resistance and the Hall effect as a function of temperature simultaneously at the 30/31 different wafer locations provided for by the lithographic pattern of Fig. 1. The system employs an electromagnet and a gas-flow cryostat designed for low vibration, fast cool down, and rapid sample mounting. Custom-built electronics and software permit simultaneous measurements of resistance and Hall coefficient to a precision of 10^{-3}. The combinatorial measurement system has been described in detail elsewhere. [17] We have recently subjected the measurement system to stringent testing for channel-to-channel reproducibility and overall resolution. Rotating the contact pattern of Fig. 1 by 180^0 reverses the channel numbering. Measuring samples in both orientations enables comparison of identical signals fed into different electrical channels. We confirmed channel-to-channel reproducibility; all the variations shown in the data come from the samples rather than the measurement system. Relative variations from channel-to-channel electronic effects have a standard deviation of $5*10^{-3}$. To test the absolute detectability, we measured the Hall effect in a 50 nm thick gold film and verified that we could resolve Hall coefficients as small as 10^{-12} m^3/C, three orders of magnitude smaller than the values typical for the optimally doped LSCO.

IV. STATISTICAL TOOLS FOR TRANSPORT CHARACTERIZATION

Having a large number, N, of measurement channels permits application of certain statistical measures. It turns out that these methods work well already for N = 30. Taken together, these

statistical measures have helped us determine precisely various contributions to the film property variations. The most useful statistical analyses have been as follows.

A. Variance-Versus-Square-Mean (VVSM) Plots

Plotting the variance of the resistance against the square of the channel-averaged resistance (with temperature as the implicit variable) yields much useful information. We estimate the true population variance, σ^2, using the discrete sample variance s^2

$$s^2 = \frac{1}{N-1}\sum_{i=1}^{N}(R_i - \bar{R})^2 \qquad (1)$$

where R_i is the resistance measured in the i^{th} channel and $\bar{R}$ is the resistance averaged over all channels. When the number of channels N is large enough, s^2 approaches σ^2, for which statistically uncorrelated fluctuations add in quadrature: $\sigma_{tot}^2 = \sigma_A^2 + \sigma_B^2$ where σ_{tot}^2 is the combined variance from independent processes denoted by the subscripts A and B. Certain types of resistance variation - lithographic patterning errors, for example - are of geometric origin and scale with the pixel resistance: $\sigma_R \sim R$. Small variations of total stoichiometry (including most notably the oxygen content) that affect the density of mobile carriers also produce pixel-to-pixel variations of resistance that scale with the overall resistance. In contrast, scattering from defects or interface roughness need not scale with R. If the spread between the channels is not large, the two types of fluctuations combine as:

$$\sigma_{tot}^2 = \sigma_0^2 + (\alpha R)^2 \qquad (2)$$

where σ_0 is the standard deviation of the resistance due to defect scattering and the last term in Eq. (2) measures the spread caused by variations in film stoichiometry and thickness and due to lithography. Plotting the variance of the resistance versus the square of the mean resistance - as suggested by Eq. 2 - yields a linear relationship with a clear distinction between the the two types of fluctuations. The slope tells us how much lithography and/or stoichiometry imperfections affect the sample; the intercept tells us about the defect density. As an example, in Fig. 2a is shown a set of R(T) characteristics of a set of pixel samples from an LSCO film patterned as described above. In Fig. 2b we show the corresponding VVSM plot, with the temperature as the implicit variable.

To differentiate between the variations in thickness, stoichiometry, and lithography, we have also utilized VVSM plots in which the statistical variable is the measured Hall voltage instead of the resistance. Because the Hall voltage scales inversely with the thickness of the film, the Hall VVSM plots place strict limits on how much the film thickness variations could contribute to the observed spread in electrical transport properties across the wafer.

B. Transverse Contact Histogram (TCH) Plots

Transverse-contact histogram (TCH) plots are a natural follow-up to the VVSM plots because they make it possible to separate the effects of lithography errors from the effects of spatial

fluctuations of total stoichiometry. They also yield crucial information about possible mechanical damage to films such as scratches caused by substrate or sample handling, micro-cracks due to mismatch in the thermal expansion coefficients of the film and the substrate, etc.

Ideally, measuring the longitudinal resistance voltage using the transverse Hall contacts, (e.g., the contacts labeled H^+ and H^- in Fig. 1) should yield zero voltage if the contacts are perfectly aligned at the opposite sides of the center conducting strip. Lithographic errors may cause contact misalignment, and this can result in non-zero voltages. Comparison with the usual (longitudinal) resistance measurements (with the distance between adjacent contact pairs fixed at 300 μm) allows us to calibrate the misalignment voltage offset. Plotting a histogram of the resistance offsets is useful because the width of distribution function provides an essential quality check on the patterning process and sets the limits on the extent to which variable sample geometry is responsible for observed pixel-to-pixel variations of measured transport properties. TCH plots showing abnormal distribution functions with long tails have been indicators of mechanical damage (such as deep scratches) in patterned films. Typical TCH plots are shown as the insets to Figs. 2b, 3b and 4b. Note that our resistance measurements are ac (usually ν = 37 Hz) and this can additionally increase the apparent resistance offset if the contact resistances are large, because of the phase lag between the two voltage pads.

C. Autocorrelation Plots

Having a large number of equally spaced probes of the sample resistance makes it possible to calculate the autocorrelation function,

$$\Xi_i = \frac{1}{s^2} < (R_i - \bar{R})(R_{i+1} - \bar{R}) > \qquad (3)$$

The autocorrelation Ξ is normalized by the sample variance s^2. The autocorrelation function filters away purely random uncorrelated channel-to-channel variation to reveal possible hidden and systematic variations of resistance across the wafer. Whereas the VVSM plots and TCH plots are useful for categorizing and quantifying different kinds of channel-to-channel variability, the autocorrelation plots help determine the physical causes of certain resistance variations.

In what follows, we show the results of such statistical analysis for three representative LSCO films patterned as shown in Fig. 1. The first, sample A (BNL film # 564) represents an early attempt to fabricate a uniform array of pixels. In this case, we used two sources for each of the metal elements (La, Sr, and Cu) oriented in opposition and with matched evaporation rates, providing the stoichiometry approximately constant along the measuring strip and the pixel array. The nominal film composition is $La_{1.80}Sr_{0.20}CuO_4$ and the film thickness is d = 32 nm. The sample B (BNL film # 721) was also targeted to be homogeneous, with the composition $La_{1.84}Sr_{0.16}CuO_4$ and the film thickness d = 53 nm. The main difference between these two samples should be in greatly improved substrate and film handling and processing in the case of sample B, as described below. The sample C (BNL film # 772) has thickness d = 43 nm and the composition $La_{1.81}Sr_{0.19}CuO_4$ at the center of the wafer. However, this film has been grown with a single Sr evaporation source aimed at 20^0 with respect to the substrate; this provides for a gradient in Sr composition across the wafer of about 4% per 1 cm as determined using QCM in situ.

The film was patterned with the pixel array oriented parallel to the Sr deposition direction, i.e., along the maximal gradient in Sr concentration.

V. ANALYSIS OF AN EARLY GROWTH SAMPLE

The temperature dependences of the resistances measured in the sample A are shown in the main panel of Fig. 2a. The relative variation among the channels at room temperature is shown in the inset. At room temperature the total channel-to-channel variation as measured by the standard deviation is 1.6%, but has a total range of 6%, which is not acceptable for our research program. Below T = 150 K, the resistance variations increase further. We consequently subjected the data of Fig. 2a to the statistical analyses described above and were able to identify the culprits and subsequently to improve growth and processing conditions.

The VVSM plot for the sample A is shown in the main panel of Fig. 2b. It indicates three different sources of resistance variations in this sample. The slope of the linear fit corresponds to the resistance variations from geometry or stoichiometry that scale with the total resistance. The intercept of the VVSM plot reveals a random amount of additional defect scattering resistance having a standard deviation of 0.87 Ω, or 0.7% of the room temperature resistance. The bump in the VVSM graph is an artifact of a single 'bad' data channel near T = 270 K. The strong increase of the variance at low resistance is not an artifact and reflects the broadening seen below T = 150 K. The upturn is likely caused by degraded electrical contacts at low temperature, as discussed below.

The TCH plot for the sample A is shown in the inset to Fig. 2b. It shows a roughly normal distribution without extended tails. The absence of long tails means that we can exclude scratches or other mechanical damage as likely contributors to the resistance variations. The width of the distribution as measured by the standard deviation and expressed as the length offset would be 1.56 µm, while our best samples usually show a width of the distribution which is ten times smaller. Local variations of the resistance, on the scale of the channel width, can randomly redirect the path of the electric current, causing random voltages between transverse contacts and increasing the width of the TCH plot. Another and likely more important factor here were large contact resistances (apparent already from Fig. 2a), as explained in Section IVB.

Compared with the 300 µm distance between adjacent contacts for resistance measurement, the randomness in apparent contact position as seen in the TCH plot provides for random resistance variations of only 0.52%. From the VVSM plot we found that the combined effects of geometry and stoichiometry contributed a total of 1.2% variation. If geometry (0.52%) and stoichiometry are uncorrelated, then the random stoichiometric variations are the dominant contribution to the resistance fluctuations at the level of 1.0%.

Autocorrelation plots are shown in Fig. 2c and 2d. For the sample A, the differences between the autocorrelation plots at T = 240 K and T = 60 K are striking. In the 240 K data, the autocorrelation cuts through randomness to reveal unexpected structure - an oscillation with a wavelength of one-half the wafer size. This may originate from a thermal gradient - e.g., due to the thermal contact between the edges of the wafer with the sample holder; this could affect the film growth and even more likely, the oxygen intake during the film cool down. Boundary conditions for

thermal processes provide for a natural length scale on the order of the wafer size. In contrast, the autocorrelation data taken at T = 60 K tell a different story. The data of Fig. 2d are consistent with white noise, i.e., with completely uncorrelated pixels. If the pixels were correlated on a length scale greater than the 300 μm contact spacing, this would be apparent in Fig. 2d. If, by contrast, the correlation length for random fluctuations were much smaller than 300 μm, then the fluctuations would have averaged out. The white noise apparent in the data suggests fluctuations on the scale of a single channel - a strong indicator of noise from degraded contact resistances at low temperature.

Enlightened by this insight, we instituted necessary changes in the growth and processing conditions for films. In the case of sample A, the gold contacts for transport measurements were evaporated ex-situ and after the film surface has been exposed to air. After the analysis presented here revealed the deleterious effect of contact resistance variations, we have adopted as the standard procedure to cover every film grown for transport studies with a thin (~10 nm thick) gold layer deposited in-situ and before any exposure of the sample to air; this improves the contacts considerably. We also lowered the temperature at which the photoresist is baked from 140 ^{0}C to 90 ^{0}C; this apparently reduced deleterious interaction between the photoresist and the near-surface layers in the film.

VI. ANALYSIS OF AN IMPROVED SAMPLE

The data and statistics for a much improved film, the sample B, are shown in Fig. 3. The main panel of Fig. 3a shows resistances with a narrower range of variation. The inset to Fig. 3a indicates that the relative variation at room temperature has a standard deviation of only 0.43% and a maximum excursion of 1.2%. We nevertheless wish to reach an even higher level of uniformity, and so have pursued an in-depth statistical analysis to characterize and further improve the growth and processing.

The VVSM plot for the sample B shown in Fig. 3b is a remarkably straight line. The intercept shows that the variation induced by defect scattering is very small, at 0.086 Ω, which is only 0.01% of the room temperature resistance. Fluctuations caused by lithography and stoichiometry together amount to 0.41% of the total resistance. The analogous VVSM plot for the Hall coefficient (not shown) also implies that the film thickness is essentially constant across the wafer.

The TCH plot for the sample B has an extremely narrow distribution with a standard deviation of only 0.15 μm as seen in the inset to Fig. 3b. No scratches or other mechanical damage are evident. In this sample, fluctuations in the measured resistance from sample geometry are less than 0.05% of the total resistance. Nearly all of the observed variations in the resistance of the sample B are caused by pixel-to-pixel variations in stoichiometry at the level of 0.41%. One would not expect such variations in the cation concentration. Under our MBE synthesis conditions, the mean free path of atoms that emanate from the evaporation sources is longer than the chamber size and the deposition is line-of-sight, with the sticking coefficients close to unity. It is thus conceivable that we may have a smooth composition gradient of the order of a per cent across the wafer due to e.g., imperfect compensation of fluxes from opposing sources. However, random variations on the scale of the pixel size (300 μm) are hardly conceivable. Under our typi-

cal growth conditions, the surface diffusion length may be of the order of 1-10 μm, so any mechanism by which the cation content could vary a lot from pixel to pixel is not obvious.

In contrast, oxygen is volatile and we have seen evidence of it diffusing slowly into or out of the LSCO sample even at room temperature, and we indeed suspect that this may be the culprit. Actually, a technique exists with which this hypothesis could be tested: Raman spectra can reveal oxygen content variation in cuprates [33], and it is possible to take such spectra even from micron-size samples. On the other hand, resonant soft X-ray scattering technique allows one to probe the mobile charge carrier density and separate its spatial variations from those in the oxygen content. [34] We hope to have such studies performed on our samples in the future.

Autocorrelation plots shown in Figs. 3c and 3d for the sample B look very similar at both T = 240 K and T = 60 K. At both temperatures, the resistance fluctuations show long range correlations, with a correlation length of nearly half the wafer size. Once again, the length scale is suggestive that thermal gradients play a role. This may be apparent from Figs. 3c and 3d which differ from what we saw earlier in the sample A. We suspect that since the sample B is far more homogeneous than previous samples, and had much smaller contact resistances, one can now discern the subtler effects of small thermal gradient across the substrate during growth. We anticipate that data like these shown in the autocorrelation plots will continue to provide essential feedback that should enable us to improve the sample homogeneity by yet another order of magnitude.

VII. ANALYSIS OF A COMBINATORIAL SAMPLE

The data and statistics for the sample C, which has a built-in 1D combinatorial spread of strontium doping level across the wafer, are shown in Fig. 4. The main panel of Fig. 4a shows the temperature dependences of the resistances in each channel. The combinatorial spread is readily apparent, with the channel dependence at room temperature plotted in the inset to Fig. 4a. The Hall effect measurements (not shown) indicate a 12% spread of total carrier density; according to the known relation between R and R_H in LSCO [35], this is fully consistent with the 9% resistance spread across the wafer.

The VVSM plot for the combinatorial the sample C shown in the main panel of Fig. 4b displays an almost linear slope that we might expect for a film with a stoichiometry gradient. It also shows an intercept associated with enhanced defect scattering. One conceivable source of this scattering may be oxygen vacancies in the CuO_2 plane, notoriously known to occur in LSCO at higher doping levels. [36] Future experimentation with different thermodynamic parameters (temperature, ozone pressure) during growth and during film post-annealing should test this hypothesis and hopefully provide a recipe for reducing this disorder.

The TCH plot in the inset to Fig. 4b has a half-width of 0.5 μm. There are no wide outliers, indicating the absence of mechanical damage to the film. The width of the TCH distribution is still much larger than might be expected from lithographic variation alone. The half-width of 0.5 μm leads us to suspect that local and random variations of total stoichiometry affect the direction of the current path in the central conducting strip, causing small random voltages in transverse contacts. This would be consistent with the conclusion of the previous paragraph.

The autocorrelation plot for the combinatorial the sample C in Fig 4c shows the intended stoichiometry gradient. Subtracting that gradient and recalculating the autocorrelation results in the data shown in Fig 4d. The autocorrelation with the gradient subtracted shows predominantly white noise, possibly with some small-scale structure similar to that seen in the uniform sample B.

VIII. CONCLUSIONS

In conclusion, we have used COMBE technique to deposit thin LSCO films with deliberate continuous spread in chemical composition (i.e., the Sr doping level) as well as nominally uniform films. We have patterned them into linear pixel arrays and used custom-made high-throughput testing techniques to accurately characterize the transport properties of each pixel. We then applied detailed statistical analysis to differentiate between various possible sources of undesirable random pixel-to-pixel variations. We have utilized this knowledge to considerably tighten the process parameters including substrate and samples handling, and significantly reduce such random variations.

The statistical data shown in Figs. 3 and 4 indicate that there is room for further improvement. The analysis of these data as presented above indicates clear directions for actions to be taken in order to achieve such improvements. One of these is to improve the temperature uniformity across the substrate during growth. The other and probably most important is to ensure uniform oxygen content. This is difficult because some (interstitial) oxygen is weakly bound and volatile even at room temperature. A solution may be to encapsulate the patterned films with some air-tight but chemically inert overlayer.

Nevertheless, it is apparent from e.g., Fig. 4a and Fig. 4c that our COMBE technique is working already. The density of data points is high enough, while the random, uncontrolled pixel-to-pixel variations are small enough to enable clear detection of major discontinuities as one would expect from quantum phase transitions.

Acknowledgment. This work has been supported by US DOE project MA-509-MACA.

References

1. S. L. Sondhi, S. M. Girvin, J. P. Carini and D. Shahar, Rev. Mod. Phys. **69**, 315 (1997).
2. S. Sachdev, Science **288**, 475 (2000).
3. Q. M. Si, S. Rabello, K. Ingersent and J. L. Smith, Nature **413**, 804 (2001).
4. S. Sachdev, Rev. Mod. Phys. **75**, 913 (2003).
5. T. Senthil, A. Vishwanath, L. Balents, S. Sachdev and M. P. A. Fisher, Science **303**, 1490 (2004).
6. M Imada, A. Fujimori and Y. Tokura, Rev. Mod. Phys. **70**, 1039 (1998).
7. Y. Tokura and N. Nagaosa, Science **288**, 462 (2000).
8. M. B. Salamon and M. Jaime, Rev. Mod. Phys. **73**, 583 (2001).

9. E. Dagotto, T. Hotta and A Moreo, Phys. Rept. **344**, 1(2001).
10. E. Dagotto, Science **309**, 5732 (2005).
11. J. L. Tallon et al., Phys. Rev. B **51**, 12911 (1995).
12. J. L. Tallon et al., Phys. Stat. Sol. B **215**, 531 (1999).
13. C. M. Varma, Phys. Rev. Lett. **83**, 3538 (1999).
14. C. Panagopoulos et al., Phys. Rev. B **66**, 064501 (2002).
15. I. Bozovic, IEEE Trans. Appl. Superconduct. **11**, 2686 (2001).
16. G. Logvenov, I. Sveklo and I. Bozovic, Physica C **460**, 416 (2007).
17. J. A. Clayhold et al., Rev. Scient. Instr. **79**, 033908 (2008).
18. P. G. Shultz and X. D. Xiang, Current Opinion is Solid State and Mat. Sci. **3**, 153 (1998).
19. X. DE. Xiang, Ann. Rev. Mat. Sci. **29**, 149 (1999).
20. X. D. Sun et al., Adv. Mat. **9**, 1046 (1997).
21. X. D. Sun et al., Appl. Phys. Lett. **70**, 3353 (1997).
22. L. F. Schneemeyer, R. B. van Dover and R. M. Fleming, Appl. Phys. Lett. **75**, 1967 (1999).
23. H. Chang et al., Appl. Phys. Lett. **72**, 2185 (1998).
24. I. Takeuchi et al., Appl. Phys. Lett. **73**, 894 (1998).
25. Y. Matsumoto et al., JJAP **38**, L603 (1999).
26. Z. W. Jin et al., Appl. Phys. Lett. **78**, 3824 (2001).
27. I. Bozovic et al., Phys. Rev. Lett. **89**, 107001 (2002).
28. I. Bozovic et al., Nature **422**, 873 (2003).
29. I. Bozovic et al., Phys. Rev. Lett. **93**, 157002 (2004).
30. N. Gedik et al., Science 316, 425 (2007).
31. A. Gozar et al., Nature **455**, 782 (2008).
32. S. Smadici et al., Phys. Rev. Lett. **102**, 107004 (2009).
33. D. Kirillov et al., Phys. Rev. B **37**, 3660 (1988).
34. P. Abbamonte et al., Science **297**, 581 (2002).
35. S. Ono, S. Komiya and Y. Ando, Phys. Rev. B **75**, 024515 (2007).
36. P. G. Radaelli et al., Phys. Rev. B **49**, 4163 (1994).

Figure captions

FIG. 1: The lithography pattern used in fabrication of linear pixel arrays. The central vertical strip, 300 μm wide and 10 mm long, is contacted from 64 square pads. The contacts divide the strip into 300 μm long segments and allow independent and simultaneous 4-point contact measurements of electrical resistance in 30 pixels and Hall effect in 31 pixels. The current leads are labeled as I^+ and I^-. The contacts labeled as R^+ and R^- are used to measure the voltage across and thus the electrical resistance of the topmost pixel. The contacts labeled as H^+ are used for Hall voltage measurement.

FIG. 2: Data and analysis for an early sample A (BNL film #564).
(a) Main panel: resistance as a function of temperature. Inset: relative variation of the resistance at room temperature.
(b) Main panel: VVSM plot quantifying contributions to the resistance fluctuations from sample geometry, stoichiometry, and defect scattering. Inset: TCH plot with a normal distribution of contact offsets.
(c) Autocorrelation plot of the resistance versus channel number at T = 240 K.
(d) Autocorrelation plot at T = 60 K showing the effects of contact degradation.

FIG. 3: Data and analysis for an improved sample B (BNL #721).
(a) Main panel: resistance as a function of temperature. Inset: relative variation of the resistance at room temperature.
(b) Main panel: VVSM plot quantifying remnant contributions to the resistance fluctuations from sample geometry, stoichiometry, and defect scattering. Inset: TCH plot with a narrow distribution showing good-quality lithography
(c) Autocorrelation plot of the resistance versus channel number at T = 240 K.
(d) Autocorrelation plot at T = 60 K.

FIG. 4: Data and analysis for the sample C (BNL #722) with built-in combinatorial spread in Sr doping level.
(a) Main panel: resistance as a function of temperature. Inset: relative variation of the resistance at room temperature.
(b) Main panel: VVSM plot quantifying remnant contributions to the resistance fluctuations from sample geometry, stoichiometry, and defect scattering. Inset: TCH plot with a narrow distribution showing good-quality lithography.
(c) Autocorrelation plot of the resistance versus channel number at T = 292 K.
(d) The same as in (c) but with the linear gradient subtracted.

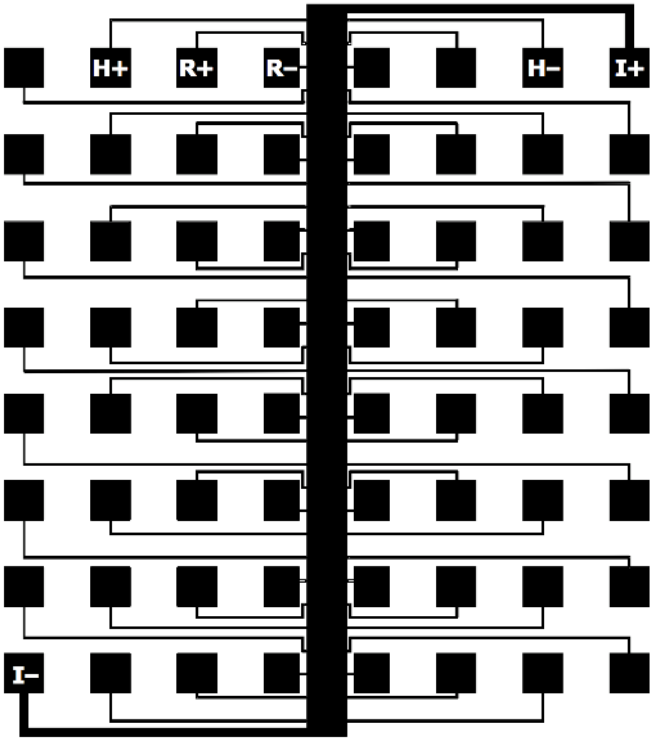

Fig. 1

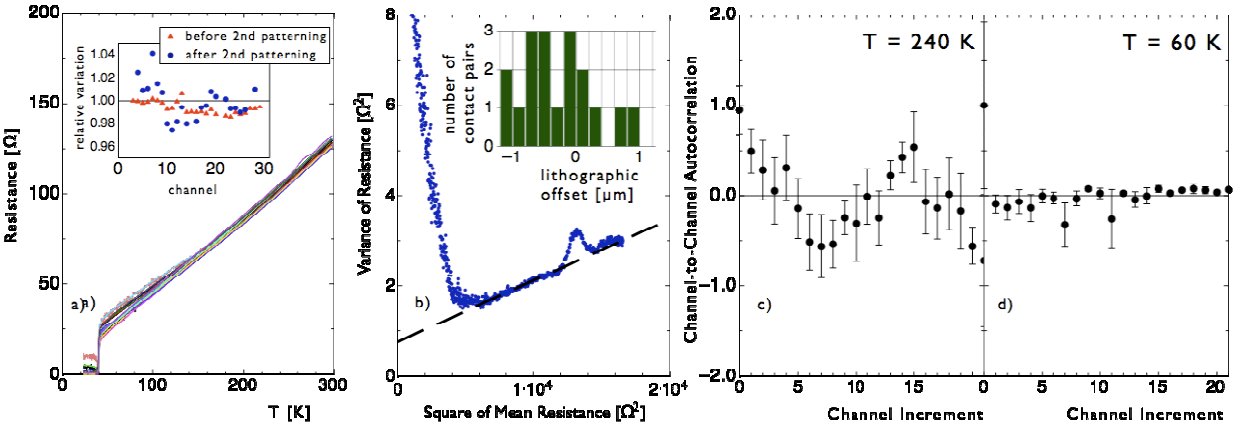

Fig. 2

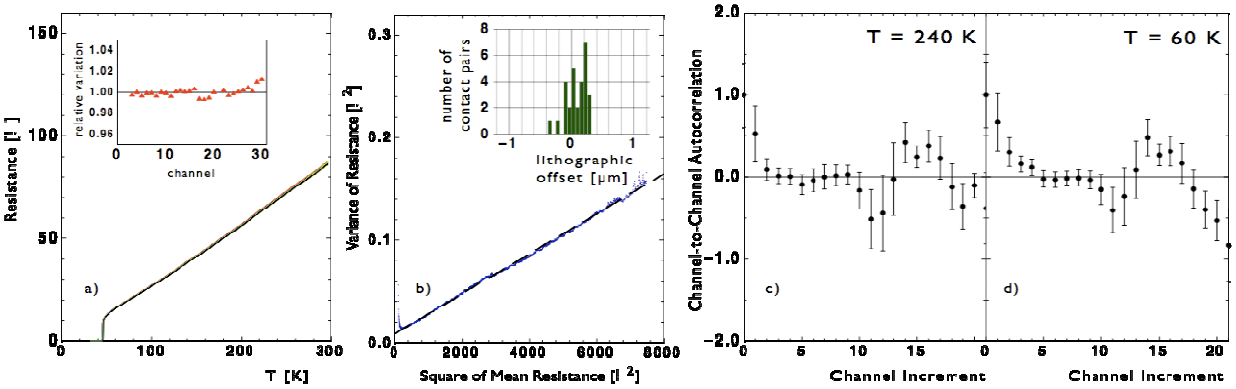

Fig. 3

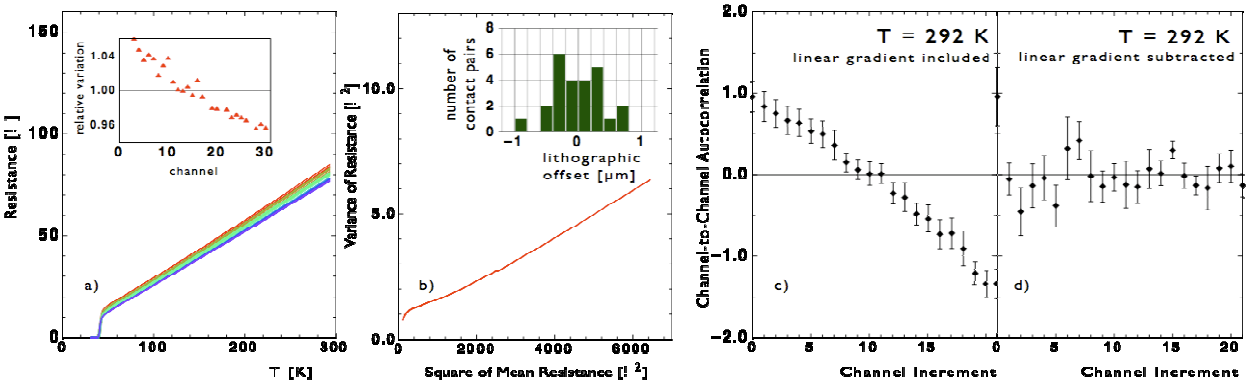

Fig. 4